JGR Space Physics

RESEARCH ARTICLE
10.1029/2018JA026158

Inferring Source Properties of Monoenergetic Electron Precipitation From Kappa and Maxwellian Moment-Voltage Relationships

Spencer M. Hatch[1], **James LaBelle**[2], **and Christopher C. Chaston**[3]

[1]Birkeland Centre for Space Science, Department of Physics and Technology, University of Bergen, Bergen, Norway, [2]Department of Physics and Astronomy, Dartmouth College, Hanover, NH, USA, [3]Space Sciences Laboratory, University of California, Berkeley, CA, USA

Key Points:
- The magnetospheric source parameters that account for observed auroral electron distributions are derived from a generalized kinetic model
- The degree of nonthermality (kappa index) in auroral primaries is required to correctly prescribe the magnetospheric source parameters
- We present the first analytical kinetic model for the relationship between density and acceleration potential along auroral field lines

Correspondence to:
S. M. Hatch,
Spencer.Hatch@uib.no

Citation:
Hatch, S. M., LaBelle, J., & Chaston, C. C. (2019). Inferring source properties of monoenergetic electron precipitation from kappa and Maxwellian moment-voltage relationships. *Journal of Geophysical Research: Space Physics*, *124*, 1548–1567. https://doi.org/10.1029/2018JA026158

Received 8 OCT 2018
Accepted 9 JAN 2019
Accepted article online 5 FEB 2019
Published online 5 MAR 2019

Abstract We present two case studies of FAST electrostatic analyzer measurements of both highly nonthermal ($\kappa \lesssim 2.5$) and weakly nonthermal/thermal monoenergetic electron precipitation at ~4,000 km, from which we infer the properties of the magnetospheric source distributions via comparison of experimentally determined number density-, current density-, and energy flux-voltage relationships with corresponding theoretical relationships. We also discuss the properties of the two new theoretical number density-voltage relationships that we employ. Moment uncertainties, which are calculated analytically via application of the Gershman et al. (2015, https://doi.org/10.1002/2014JA020775) moment uncertainty framework, are used in Monte Carlo simulations to infer ranges of magnetospheric source population densities, temperatures, κ values, and altitudes. We identify the most likely ranges of source parameters by requiring that the range of κ values inferred from fitting experimental moment-voltage relationships correspond to the range of κ values inferred from directly fitting observed electron distributions with two-dimensional kappa distribution functions. Observations in the first case study, which are made over ~78–79° invariant latitude in the Northern Hemisphere and 4.5–5.5 magnetic local time, are consistent with a magnetospheric source population density $n_m = 0.7$–0.8 cm^{-3}, source temperature $T_m \approx 70$ eV, source altitude $h = 6.4$–$7.7\ R_E$, and $\kappa = 2.2$–2.8. Observations in the second case study, which are made over 76–79° invariant latitude in the Southern Hemisphere and ~21 magnetic local time, are consistent with a magnetospheric source population density $n_m = 0.07$–0.09 cm^{-3}, source temperature $T_m \approx 95$ eV, source altitude $h \gtrsim 6\ R_E$, and $\kappa = 2$–6.

Plain Language Summary The plasma sheet is the magnetospheric source region for much of the electron precipitation that produces aurora several thousand kilometers below, within the ionosphere at approximately 100 km altitude on Earth's nightside. Using FAST satellite observations within the so-called magnetosphere-ionosphere transition region, we show how the features of these accelerated, aurora-forming electrons as observed by satellites at intermediate altitudes can be used to infer the density, temperature, degree of thermal equilibration, and altitude of the magnetospheric source region.

1. Introduction

Potential differences exist along geomagnetic field lines that connect the plasma sheet and high-latitude magnetosphere to the ionosphere. Knight (1973) formally demonstrated the relationship between a field-aligned, monotonic potential profile represented by a total potential difference $\Delta\Phi$ and field-aligned current density below the potential drop $j_\parallel$ generated by precipitation of magnetospheric electrons subject to a magnetic mirror ratio $R_B = B/B_m$,

$$j_{\parallel,M}(\Delta\Phi; T_m, n_m, R_B) = -en_m\left(\frac{T_m}{2\pi m_e}\right)^{\frac{1}{2}} R_B\left[1-\left(1-R_B^{-1}\right)\exp\left\{-\frac{\bar{\phi}}{(R_B-1)}\right\}\right]. \quad (1)$$

Here T_m and n_m are the temperature and density of precipitating electrons at the magnetospheric source, $\bar{\phi} \equiv e\Delta\Phi/T_m$ is the potential drop normalized by source temperature, and m_e is the electron mass. The subscript m indicates the magnetospheric source region.

©2019. The Authors.
This is an open access article under the terms of the Creative Commons Attribution-NonCommercial-NoDerivs License, which permits use and distribution in any medium, provided the original work is properly cited, the use is non-commercial and no modifications or adaptations are made.

The current density-voltage (J-V) relation (1) assumes that the magnetospheric source population is isotropic and in thermal equilibrium, and is thus described by a Maxwellian distribution. However, magnetospheric electron and ion distributions observed with spacecraft often show suprathermal tails (Christon et al., 1989, 1991; Kletzing et al., 2003; Wing & Newell, 1998) which may be produced via a number of mechanisms (see, e.g., review by Pierrard & Lazar, 2010). The possibility of a source distribution with a "high-energy tail" was in fact acknowledged by Knight (1973), and reformulations of the Maxwellian J-V relation (1) assuming a variety of alternative source distributions have been developed (Boström, 2003, 2004; Dors & Kletzing, 1999; Janhunen & Olsson, 1998; Pierrard, 1996). One such alternative distribution employed with increasing frequency is the isotropic kappa distribution

$$f_\kappa(E;T,n,\kappa) = n\left(\frac{m}{2\pi T(1-\frac{3}{2\kappa})}\right)^{\frac{3}{2}} \frac{\Gamma(\kappa+1)}{\kappa^{3/2}\Gamma\left(\kappa-\frac{1}{2}\right)}\left(1+\frac{E}{\left(\kappa-\frac{3}{2}\right)T}\right)^{-1-\kappa}, \tag{2}$$

which originally entered the space physics community as a model for high-energy tails of observed solar wind plasmas (Vasyliūnas, 1968). The additional parameter $\kappa \in \left[\kappa_{\min}, \infty\right)$ parameterizes the degree

$$\rho = \kappa_{\min}/\kappa \in (0,1] \tag{3}$$

to which particle motion is correlated and is related to the "thermodynamic distance" between a stationary (i.e., invariant over relevant time scales) nonequilibrium state and thermal equilibrium. The range of κ values observed in a plasma environment depends on the transport, wave-particle interaction, and acceleration processes that are found within that environment (see, e.g., Pierrard & Lazar, 2010; Treumann, 1999b). The theoretical minimum (in three dimensions) $\kappa_{\min} = 3/2$ corresponds to perfectly correlated degrees of freedom and particle motions ($\rho = 1$), while $\kappa \to \infty$ corresponds to uncorrelated degrees of freedom ($\rho = 0$) and thermal equilibrium, or a Maxwellian distribution (Treumann, 1999a).

Livadiotis and McComas (2010) have shown that $\kappa_t \simeq 2.45$ ($\rho \simeq 0.61$) marks a transition between these two extremes, with $\kappa_{\min} \leq \kappa \lesssim \kappa_t$ constituting the "far-equilibrium" regime and $\kappa_t \lesssim \kappa < \infty$ the "near-equilibrium" regime.

Relaxing the assumption of a magnetospheric source population in thermal equilibrium, Dors and Kletzing (1999) showed that the J-V relation (1) becomes

$$\begin{aligned} j_{\parallel,\kappa}(\Delta\Phi;T_m,n_m,\kappa,R_B) = &-en_m\left(\frac{(1-\frac{3}{2\kappa})T_m}{2\pi m_e}\right)^{1/2} \frac{\Gamma(\kappa+1)}{\kappa^{3/2}\Gamma(\kappa-\frac{1}{2})}\frac{R_B}{1-1/\kappa} \\ &\times\left[1-\left(1-R_B^{-1}\right)\left(1+\frac{\bar{\phi}}{(\kappa-\frac{3}{2})(R_B-1)}\right)^{1-\kappa}\right]. \end{aligned} \tag{4}$$

For equal n_m and T_m, the values of $j_\parallel$ predicted by equations (1) and (4) differ by more than ~33% for the far-equilibrium regime ($\kappa_{\min} < \kappa \lesssim \kappa_t$; Hatch et al., 2018). Recent case studies (Kaeppler et al., 2014; Ogasawara et al., 2017) and a statistical study (Hatch et al., 2018) suggest that such extreme κ values seldom occur in the auroral acceleration region.

Equations (1), otherwise known as the Knight relation, and (4) are examples of J-V relationships. Such relationships are a means for understanding the role of field-aligned potential differences within large-scale magnetospheric current systems. The Knight relation in particular has contributed to present understanding of the magnetosphere-ionosphere current system (e.g., Boström, 2003; Cowley, 2000; Dombeck et al., 2013; Karlsson, 2012; Lu et al., 1991; Lyons et al., 1999; Paschmann et al., 2003; Pierrard et al., 2007; Shiokawa et al., 1990; Temerin, 1997). Moment-voltage relationships such as that between energy flux and voltage, a "J_E-V" relationship, are also derivable (Boström, 2003, 2004; Chiu & Schulz, 1978; Dors & Kletzing, 1999; Janhunen & Olsson, 1998; Liemohn & Khazanov, 1998; Pierrard, 1996; Pierrard et al., 2007). These other relationships have received comparatively little attention even though they represent additional, valuable tools for estimating magnetospheric source population parameters from particle observations at lower altitudes.

Using previously published J-V and J_E-V relationships and two new number density-voltage (n-V) relationships, we show how knowledge of the degree to which monoenergetic precipitation departs from Maxwellian form leads to identification of narrow ranges of magnetospheric source parameters that are

compatible with observed moment-voltage relationships. This technique is enabled by the Gershman et al. (2015) methodology for analytic calculation of moment uncertainties as well as direct two-dimensional distribution fits.

2. Methodology

Here we summarize the J_E-V and n-V relationships that we use in addition to the J-V relationships (1) and (4), as well as the Gershman et al. (2015) methodology for estimating moment uncertainties of measured electron distribution functions.

2.1. J_E-V and n-V Relationships

Assuming a monotonic potential profile the J_E-V relationships for isotropic Maxwellian and kappa source distributions are, respectively (Dors & Kletzing, 1999),

$$j_{E\|,M} = \frac{n_m T^{3/2}}{\sqrt{2\pi m_e}} R_B \left\{ (2+\bar{\phi}) - \left[\bar{\phi} + 2\left(1 - R_B^{-1}\right)\right] \exp\left(\frac{-\bar{\phi}}{R_B - 1}\right) \right\} \tag{5}$$

and

$$\begin{aligned} j_{E\|,\kappa} = {} & n_m \frac{\left[\left(1-\frac{3}{2\kappa}\right)T_m\right]^{3/2}}{\left(2\pi m_e\right)^{1/2}} \frac{\kappa^2}{\kappa^{3/2}(\kappa-1)(\kappa-2)} \frac{\Gamma(\kappa+1)}{\Gamma\left(\kappa-\frac{1}{2}\right)} R_B \left\{ \left[2 + \frac{\kappa-2}{\kappa-3/2}\bar{\phi}\right] \right. \\ & -\Pi^{-\kappa+1}\left(1 - R_B^{-1}\right)\left(\frac{\kappa-2}{\kappa-1} + \frac{\kappa-2}{\kappa-3/2}\bar{\phi}\right)\left(\frac{\kappa}{(\kappa-1)(R_B-1)} + 1\right) \\ & \left. -\Pi^{-\kappa+2}\left(1 - R_B^{-1}\right)^2\left(1 + \frac{1+\kappa/(R_B-1)}{\kappa-1}\right)\right\}, \end{aligned} \tag{6}$$

with $\Pi = 1 + \frac{\bar{\phi}}{(\kappa-3/2)(R_B-1)}$ in (6). One may also derive the corresponding Maxwellian and kappa n-V relationships (Appendix A)

$$n_M(\Delta\Phi; T_m, n_m, R_B) = n_m \left[\frac{1}{2} e^{\bar{\phi}} \mathrm{erfc}\left(\sqrt{\bar{\phi}}\right) + \sqrt{\frac{R_B - 1}{\pi}} D\left(\sqrt{\frac{\bar{\phi}}{R_B - 1}}\right)\right]; \tag{7}$$

$$\begin{aligned} n_\kappa(\Delta\Phi; T_m, n_m, R_B, \kappa) = {} & n_m \frac{\bar{\phi}^{3/2}}{\sqrt{\pi}(\kappa - \frac{3}{2})^{3/2}} \frac{\Gamma(\kappa+1)}{\Gamma(\kappa - 1/2)} \\ & \times \left[\int_0^\infty dx \sqrt{1+x}\left(1 + \frac{x\bar{\phi}}{\kappa - \frac{3}{2}}\right)^{-\kappa-1} \right. \\ & \left. - \frac{1}{R_B - 1}\int_0^1 dx \sqrt{1-x}\left(1 + \frac{x\bar{\phi}}{\left(\kappa - \frac{3}{2}\right)(R_B - 1)}\right)^{-\kappa-1}\right]; \end{aligned} \tag{8}$$

where $D(y) = \exp\left(-y^2\right)\int_0^y \exp\left(y'^2\right) dy'$ in (7) and x is a dummy integration variable in (8). The relationships (5)–(8) are written in terms of the same variables as those used in the J-V relationships (1) and (4). Properties of the J_E-V relationships (5) and (6) have been discussed by Dors and Kletzing (1999). Some properties of the n-V relationships (7) and (8), which are previously unpublished, are discussed here.

Figure 1a shows the n-V relationships as a function of $\bar{\phi}$ for Maxwellian ($\kappa \to \infty$, orange lines), moderately nonthermal ($\kappa = \kappa_t$, blue lines), and extremely nonthermal ($\kappa = 1.6$, blue lines) source populations. Mirror ratios of 3, 30, and 300 are represented by solid, dashed, and dotted lines respectively.

It is evident that $n/n_m \to 1/2$ in the limit $\bar{\phi} \to 0$; this behavior is shown analytically for the Maxwellian n-V relation in the asymptotic expression (A3). On the other hand, $n/n_m \to 0$ for $\bar{\phi} \gg R_B$, as shown in the asymptotic expression (A4).

The n-V relationships predict half the source density n_m in the $\bar{\phi} \to 0$ limit (i.e., no field-aligned potential) because only those particles in the magnetospheric source region having a parallel velocity component toward the ionosphere (defined as $v_\| > 0$) are included in the range of integration used to obtain the n-V relationships; all others move away from the ionosphere and are ignored (Appendix A). This restriction on

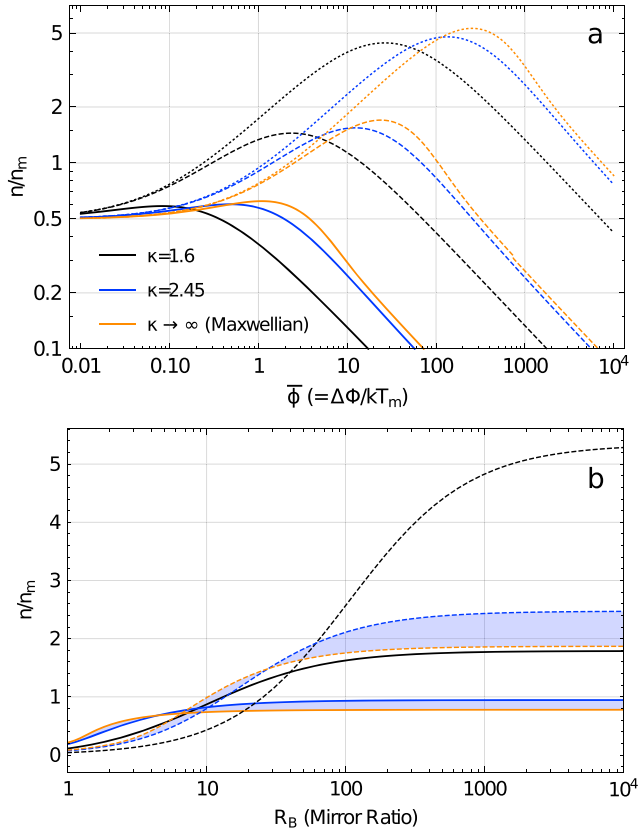

Figure 1. The n-V relationships in equations (7) and (8). The ratio n/n_m is plotted on the y axis, where n_m is magnetospheric source population density and n is the density at the altitude corresponding to mirror ratio R_B and to the bottom of normalized potential drop $\bar{\phi} = \Delta\Phi/T_m$. (a) n-V relationships as a function of $\bar{\phi}$ for $R_B = 3$ (solid lines), $R_B = 30$ (dashed lines), and $R_B = 300$ (dotted lines). (b) n-V relationships as a function of R_B for $\bar{\phi} = 1$ (solid lines) and $\bar{\phi} = 10$ (dashed lines). In panel (b) the region between the $\kappa = \kappa_t$ and $\kappa \to \infty$ curves is shaded. n-V = number density-voltage.

the range of integration is identically the reason that in the $\bar{\phi} \to 0$ limit the J-V relations (1) and (4) and the J_E-V relationships (5)–(6), respectively, predict nonzero current densities, or "thermal flows" (Paschmann et al., 2003), and nonzero energy fluxes. For instance, in this limit $j_{\parallel,M} = -en_m(T_m/2\pi m_e)^{1/2}$. (See, e.g., Figure 3.8 in Paschmann et al., 2003).

More generally, increasing $\bar{\phi}$ (i) increases the number of particles that have access to lower altitudes by increasing $v_\parallel$, which increases n/n_m (the total volume under the distribution function), and (ii) compresses the distribution function in velocity space (see Inequality (A2a)), which decreases n/n_m. On the other hand, increasing R_B while simultaneously conserving the first adiabatic invariant causes the distribution function to evolve toward an annular or "ring" distribution, such that (i) particles at large pitch angles ($v_\perp > v_\parallel$) in the source region are reflected at lower altitudes, which decreases n/n_m, and (ii) particles with small pitch angles ($v_\parallel > v_\perp$) in the source region, particularly those near the peak of the distribution near $v_\parallel = \sqrt{2e\Delta\Phi/m}$, also spread to larger pitch angles, increasing the total volume under the distribution function and thereby increasing n/n_m. The maximum values of n/n_m in Figure 1a thus represent nontrivial interplay of these competing factors (see equation (A5)).

Figure 1b shows as a function of R_B the Maxwellian and kappa n-V relationships (7) and (8) normalized by source density n_m, for $\bar{\phi} = 1$ (solid lines), $\bar{\phi} = 10$ (dashed lines), and several values of κ. The magnetospheric source region corresponds to $R_B = 1$. For a Maxwellian source population in the limit $R_B \to 1$, n is given by the first term in the Maxwellian n-V relation (7). For a kappa source population in the limit $R_B \to 1$, n approaches values similar to that approached by the Maxwellian curve. The topmost curve in Figure 1b shows that for $\bar{\phi} = 10 \ll R_B$ and $\kappa = 1.6$, the density at lower altitudes increases by as much as a factor 5. More generally, $n/n_m \propto \sqrt{\bar{\phi}/(1 - \frac{3}{2\kappa})}$ for $1 \lesssim \bar{\phi} \ll R_B$. The shaded region between the $\kappa = \kappa_t$ and $\kappa \to \infty$

curves (blue and orange, respectively) in Figure 1b indicates that there is little difference, generally less than 30%, between the Maxwellian and kappa n-V relationships for $\kappa \gtrsim \kappa_t$ and equal $\bar{\phi}$. Asymptotic expressions for the Maxwellian n-V relation (7) are given in Appendix A.

2.2. Uncertainty of Distribution Moments

This study also relies on moments of measured electron distributions, including the number density n, field-aligned current density $j_{\parallel} = e\langle nv_{\parallel}\rangle$, and field-aligned energy flux $j_{E\parallel} = \frac{m}{2}\langle nv^2 v_{\parallel}\rangle$. Estimation of the uncertainty of moments has typically involved generation of statistics of each moment via Monte Carlo simulation of $f(\mathbf{v})$ (e.g., Moore et al., 1998). We alternatively use standard techniques of linearized uncertainty analysis to derive analytic expressions for the uncertainties of field-aligned current density and energy flux, respectively, $\sigma_{j_{\parallel}}$ and $\sigma_{j_{E\parallel}}$, as functions of moments of $f(\mathbf{v})$ and moment covariances. (The uncertainty of number density n is trivially σ_n.) Moment covariances are calculated following the methodology of Gershman et al. (2015). In Appendix B we present both these analytic expressions and a summary of the Gershman et al. (2015) methodology, which together enable the Monte Carlo simulations presented in sections 3.2 and 4.2.

3. Orbit 1607

3.1. Data Presentation

During an approximately 90-s interval on 17 January 1997, the FAST satellite observed inverted V electron precipitation over 80–600 eV (Figures 2a and 2b) and over ~4.5–5.5 magnetic local time in the Northern Hemisphere during low geomagnetic activity ($K_p = 0^-$). Figure 2a shows that over much of this interval the distributions include both isotropic and trapped components, while the antiearthward loss cone is relatively depleted. For instance over 01:05:10–01:05:15 UT the isotropic component is somewhat weak ($dJ_E/dE \lesssim 3 \times 10^7$eV/cm^2-s-sr-eV) and the trapped component is more intense ($dJ_E/dE \gtrsim 10^8$eV/cm^2-s-sr-eV).

Figure 2b gives the observed electron energy spectrogram averaged over observations at all pitch angles within the earthward loss cone. The loss cone is calculated from model geomagnetic field magnitudes at FAST and at the 100-km ionospheric footpoint, which are both obtained from International Geomagnetic Reference Field 11. For the period indicated between dashed lines (01:04:28–01:04:41 UT), which we will discuss momentarily, Figure 2b shows that the peak energy of monoenergetic electron precipitation varies between 80 and 500 eV.

We perform full 2-D fits to the portion of electron distributions that are observed within the earthward loss cone (horizontal dotted white lines in Figure 2a) and between the energy at which the distributions peak above 80 eV (E_p) up to the 30-keV limit of FAST electron electrostatic analyzers (EESAs; Carlson et al., 2001). To obtain these fits, we first form a 1-D differential number flux distribution by averaging the counts within each EESA energy-angle bin over the range of angles within the earthward portion of the loss cone, after which 1-D fits of the resulting average differential number flux spectrum are performed using the model differential number flux $J = \frac{2E}{m^2} f\left(E - E_p\right)$, with $f\left(E - E_p\right)$ either a 1-D Maxwellian or 1-D kappa distribution. The resulting 1-D best-fit parameters then serve as initial estimates for 2-D fits of the observed differential energy flux spectrum, over the previously described range of pitch angles and energies, using model differential energy flux $dJ_E/dE = \frac{2E^2}{m^2} f\left(E - E_p\right)$. Both 1-D and 2-D distribution fits are performed using Levenberg-Marquardt weighted least-squares minimization via the publicly available Interactive Data Language MPFIT library (http://cow.physics.wisc.edu/~craigm/idl/fitting.html).

The most probable fit parameters and 90% confidence intervals are then obtained by following a procedure similar to those employed by Kaeppler et al. (2014) and Ogasawara et al. (2017): for each time and each type of distribution, we fit $N = 5{,}000$ Monte Carlo simulated 2-D distributions by adding to each best-fit distribution a normal random number $Z \sim \mathcal{N}(0, 1)$ that is multiplied by the counting uncertainty (section 15.6 in Press et al., 2007) in units of differential energy flux. For the simulated kappa distribution fits we also select a uniform random number $K \sim U(\kappa_{\min}, 35)$ as an initial guess for κ.

For each fit parameter we then form a histogram from the resulting 5,000 Monte Carlo values. The value at which the histogram peaks is taken to be the most probable fit parameter. We then use a simple algorithm that increases the size of a window centered on the most probable fit parameter until 4,500 (90%) of the parameter values are included in the window.

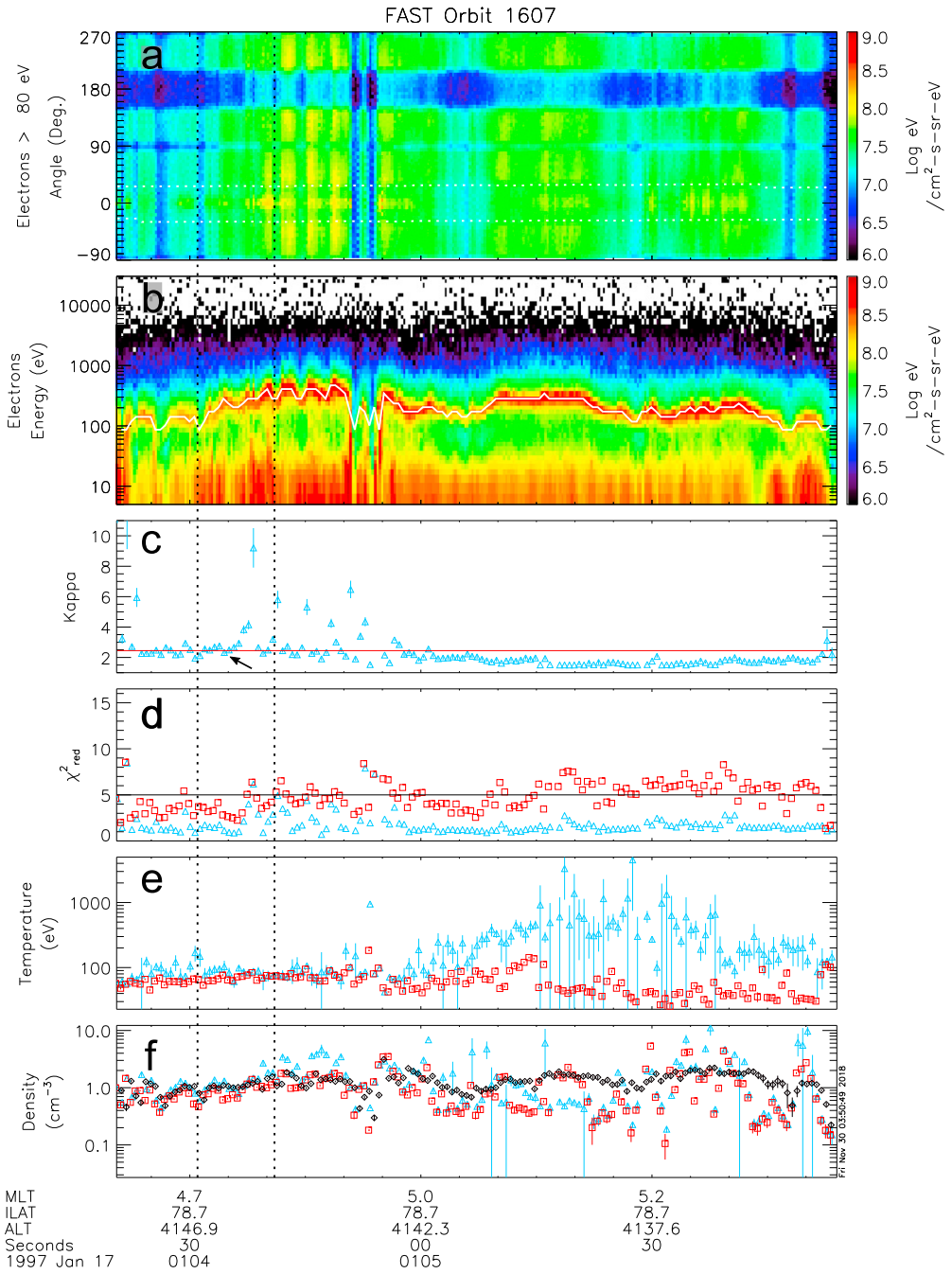

Figure 2. Electron electrostatic analyzer observations of inverted V precipitation on 17 January 1997, and corresponding 2-D fit parameters. Parameters related to best-fit Maxwellian and kappa distributions are, respectively, indicated by red squares and blue triangles in panels (c)–(f). (a) >80-eV electron pitch-angle distribution. The earthward portion of the loss cone (see text for definition) comprises the ~60° range of pitch angles between the dotted horizontal lines at approximately 30° and approximately −30°. (b) Average electron energy spectrum within the earthward loss cone. (c) κ fit parameter for the best-fit kappa distribution. The red horizontal line indicates $\kappa = \kappa_t \simeq 2.45$. The black arrow indicates the kappa value for fits shown in Figure 3. (d) Reduced chi-squared statistic χ^2_{red} for each fit type. The black horizontal line indicates $\chi^2_{\mathrm{red}} = 5$. (e) Best-fit temperatures. (f) Calculated density moments (black diamonds) and best-fit densities. Calculated densities are obtained as 2-D model-independent moments of the differential flux measured over pitch angles $|\theta| \leq 30°$, from the energy of the channel immediately below the peak energy E_p up to 5 keV. Resulting density moments and uncertainties (vertical black bars) are then multiplied by the ratio of the solid-angle ratio $1/(1 - \cos 30°) \approx 7.46$. Uncertainties of best-fit parameters represent 90% confidence intervals obtained via Monte Carlo simulations with $N = 5{,}000$ trials. Electron electrostatic analyzer observations are integrated to obtain an effective sample period $T = 0.63$ s. MLT = magnetic local time; ILAT = invariant latitude.

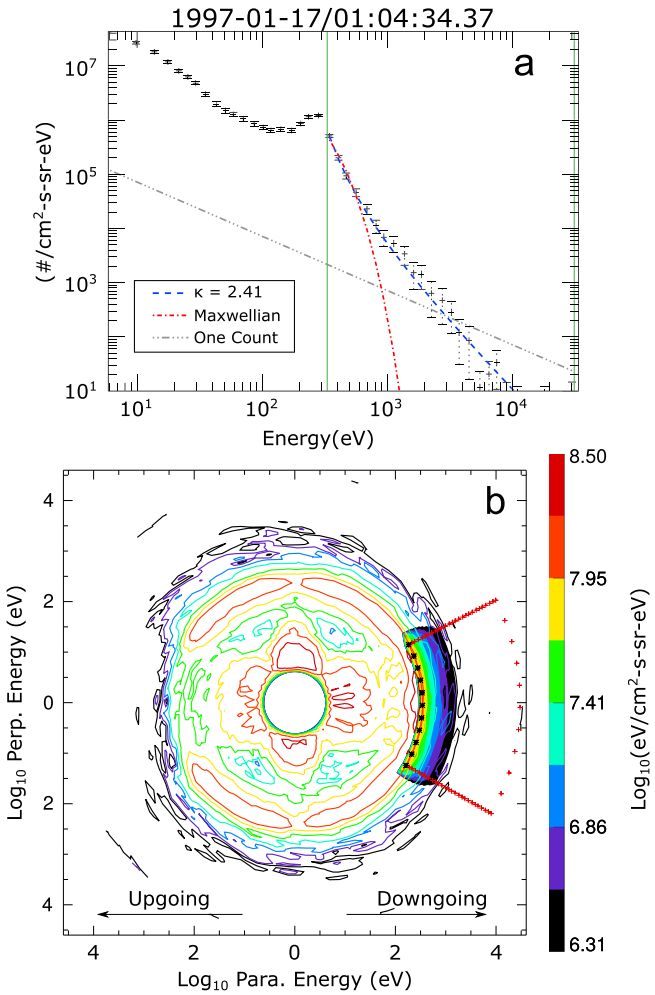

Figure 3. Electron spectra observed at 01:04:34.37–01:04:35.00 UT. (a) 1-D differential number flux spectrum (black crosses) obtained by averaging differential number flux spectra over all pitch angles within the earthward loss cone, with best-fit Maxwellian and kappa distributions overlaid (red dash-dotted line and blue dashed line, respectively). The uncertainty of each observed differential number flux is calculated by conversion of the electron count uncertainty $\sqrt{N}$ to units of differential number flux. (b) Best-fit 2-D kappa distribution (solid contours) with the observed 2-D differential energy flux spectrum overlaid (contour lines). The color bar at right shows the differential energy flux of each contour. For each pitch angle black asterisks indicate the peak energy $E_p = 315$ eV, and red plus signs outline the range of energies and pitch angles used to perform the 2-D fit.

Reported parameters are κ (Figure 2c) for the kappa distribution, and temperature (Figure 2e) and density (Figure 2f) for both Maxwellian and kappa distribution fits. For each most probable fit parameter the 90% confidence interval is indicated by a vertical bar. In many instances the upper and lower limits of the 90% confidence interval are very near the most probable fit parameter value. For example, for over 92% of the most probable κ parameters in Figure 2c the upper and lower limit of the 90% confidence interval is within 10% of the most probable κ parameter itself.

Figure 3 shows example 1-D (Figure 3a) and 2-D (Figure 3b) distribution fits to electron observations during 01:04:34.37–01:04:35.00 UT, indicated by the black arrow in Figure 2c. The observed distribution in Figure 3a (black plus signs and error bars) is much better described by the best-fit kappa distribution (blue dashed line) than by the best-fit Maxwellian distribution (red dash-dotted line). The overall better description that the kappa distribution fits yield for observations throughout the entire 90-s interval is indicated in Figure 2d, which shows values of the reduced chi-squared statistic

$$\chi^2_{\text{red}} = \sum_i^N \frac{1}{F} \frac{\left(Y_i(x) - y_i(x)\right)^2}{w_i^2} \tag{9}$$

for 2-D fits using either a kappa distribution (blue triangles) or a Maxwellian distribution (red squares). In this expression i indexes each pitch angle and energy bin used in the fitting procedure, Y_i is the observed differential energy flux, y_i is the differential energy flux of the original best-fit 2-D model distribution, w_i is the uncertainty due to counting statistics, and F is the degrees of freedom, or the total number of pitch angle-energy bins N minus the number of free model parameters. The difference is most pronounced after approximately 01:05:00 UT, corresponding to the interval during which $\kappa_{\min} < \kappa \lesssim 2$ in Figure 2c.

Figure 2e shows that over approximately the first half of the 90-s interval, $T = 30$–200 ev for both Maxwellian and kappa distribution fits. Comparison with statistical plasma sheet temperatures reported by Kletzing et al. (2003, their Figure 4) indicates that these temperatures are within typical ranges. During the latter half of the interval the most probable kappa temperatures tend to be much higher (~100–2000 eV) than during the first half, while corresponding Maxwellian temperatures remain low (20–100 eV). The kappa "core temperatures" (Nicholls et al., 2012) $T_c = T(1 - \frac{3}{2\kappa})$ (not shown) during the latter half are nonetheless within several eV of Maxwellian temperatures.

Figure 2f shows that relative to the calculated densities, the best-fit densities for Maxwellian and kappa distributions are generally within factors of two to five. For calculated densities the corresponding uncertainties (vertical black bars) are obtained using analytic expressions for moment uncertainties related to counting statistics for an arbitrary distribution function (Gershman et al., 2015). These uncertainties are generally less than 10% of the calculated density.

3.2. Inference of Magnetospheric Source Parameters

We now demonstrate how the observed electron distributions may indicate the properties of the magnetospheric source region. This is performed via comparison of the predictions of moment-voltage relationships (1) and (4)–(8) with experimental moment-voltage relationships derived from model-independent fluid moments of the electron distributions observed during the delineated interval between dashed lines in Figure 2, 01:04:31–01:04:41 UT. We have selected this interval because it is associated with the largest variation in the inferred potential during the entire 90-s period.

The J-V and J_E-V relationships are formed by first determining the potential drop $\Delta\Phi$ (solid white line, Figure 2b) at each time, which is taken to be the peak electron energy E_p. (There is no potential drop below FAST during this interval, which would otherwise be indicated by the presence of upgoing ion beams; see, e.g., Elphic et al., 1998; Hatch et al., 2018). We define the peak energy E_p as the energy of the EESA channel above which the observed differential flux spectrum exhibits exponential or power law decay (Kaeppler et al., 2014; Ogasawara et al., 2017), within the earthward loss cone. We then calculate the parallel electron current density $j_{\|,i}$ and energy flux $j_{E\|,i}$ of the observed electron distribution, using measurements from the peak energy E_p up to 5 keV and the range of angles within the earthward loss cone. The upper bound of the energy integration range is limited to 5 keV because statistics of particles above this energy are poor and contribute almost exclusively to the uncertainty of these moments. These two moments are mapped to the ionosphere at 100 km using International Geomagnetic Reference Field 11 (denoted by the subscript i).

The n-V relationship is also formed from the inferred potential drop $\Delta\Phi$ and from the calculated number density n, but unlike the fluxes $j_{\|,i}$ and $j_{E\|,i}$, n is not a flux and is not straightforward to map to the ionosphere. We therefore must form a "local" (i.e., unmapped) n-V relationship and obtain n via integration over the same range of energies that are used to calculate $j_{\|,i}$ and $j_{E\|,i}$ (from E_p up to 5 keV), but over a modified pitch angle range, which in a local treatment should be the full 180° range of earthward pitch angles. However, inspection of the delineated interval in Figure 2a indicates the presence of a prominent trapped population at pitch angles $|\theta| \gtrsim 40°$ (e.g., at 01:04:37 UT) that should not be included in the calculation of n. We therefore integrate over a 60° range of angles that is centered on the earthward loss cone and multiply both the calculated densities and their uncertainties by the solid-angle ratio $1/(1 - \cos 30°) \approx 7.46$ to compensate for the exclusion of observations over pitch angles $|\theta| > 30°$. This multiplication assumes the primary electron distribution is isotropic outside the loss cone.

The experimental J-V, J_E-V, and n-V relationships are shown in Figures 4a–4c. Also shown are the results of simultaneously fitting all three of these relationships with the corresponding Maxwellian and kappa moment-voltage relationships (1)–(8) using NonlinearModelFit in the Mathematica® (v11.3) programming language. The best-fit Maxwellian (blue lines) and kappa (orange lines) fits correspond to $\chi^2_{\text{red}} = 25.2$ and

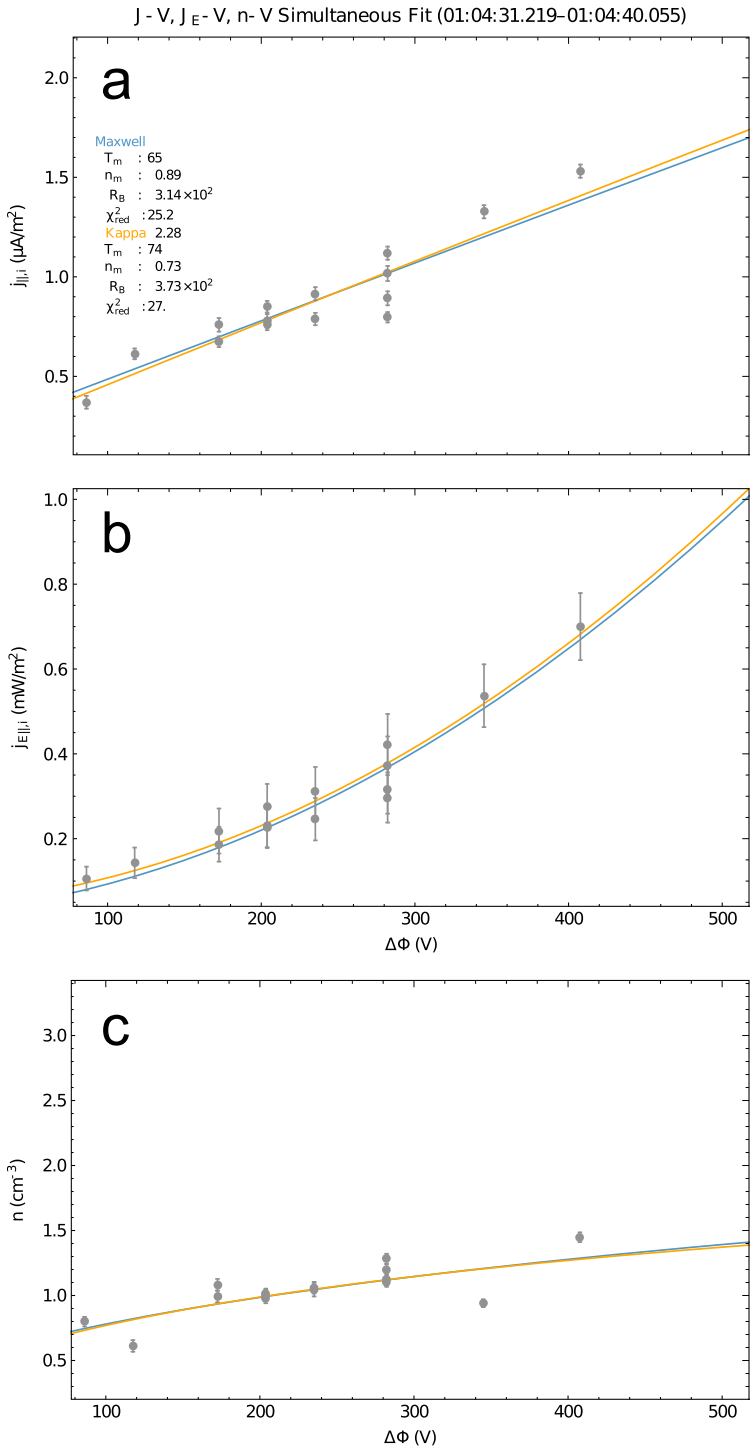

Figure 4. J-V, J_E-V, and n-V relationships inferred from electron observations during the interval 01:04:28–01:04:41 UT in Figure 2, together with best-fit Maxwellian (solid blue lines) and kappa (solid orange lines) moment-voltage relationships obtained by simultaneously fitting all three experimentally inferred moment-voltage relationships. (a) J-V relationship. (b) J_E-V relationship. (c) n-V relationship. Given values of the inferred potential drop ΔΦ occur multiple times within the sample interval, causing the experimental data to be multivalued. Calculated current densities and energy fluxes (bullets) as well as their uncertainties (1σ) are mapped to the ionosphere at 100 km as described in the text. Calculated number densities are not mapped to the ionosphere. Moment uncertainties are obtained as analytic moments of observed electron distributions, as described in Appendix B. The χ^2_{red} values indicated in Figure 4a are the sum of the χ^2_{red} value corresponding to each moment-voltage relationship. J-V = current density-voltage; J_E-V = energy flux-voltage; n-V = number density-voltage.

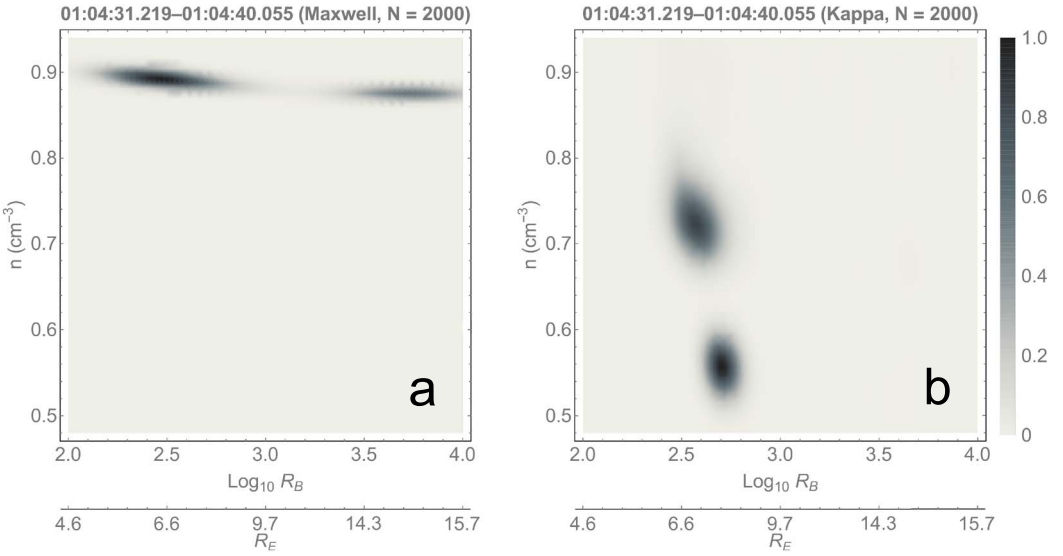

Figure 5. (a) Joint distribution of density n_m and mirror ratio R_B for Maxwellian fits of $N = 2{,}000$ Monte Carlo simulated current density-voltage, energy flux-voltage, and number density-voltage relationships (1), (5), and (7). (b) Same as panel (a), except that fits are performed using the kappa current density-voltage, energy flux-voltage, number density-voltage relationships (4), (6), and (8). In both panels the R_B axis is logarithmic and the secondary axis shows the approximate source height h in Earth radii. The gray scale indicates the distribution height in units such that the peak value of each distribution is 1.0.

$\chi^2_{\text{red}} = 27$, respectively, where these two χ^2_{red} values are the sum of the three χ^2_{red} corresponding to each type of moment-voltage relation.

We obtain these fits by drawing from random variables $N \sim U(0.05\ \text{cm}^{-3}, 1.5\ \text{cm}^{-3})$ and $R \sim U(5, 10^4)$ to initialize n_m and R_B in each moment-voltage relationship. For the kappa moment-voltage relationships we must also draw from a random variable to initialize the κ parameter. To accomplish this we randomly choose a degree of correlated motion $W \sim U(0.05, 0.85)$ (see equation (3)), from which we obtain an initial kappa value $K \sim \kappa_{\min}/W$. The lower and upper bounds of the uniformly random degree of correlation W, $\rho = 0.05$ and $\rho = 0.85$, respectively, correspond to $\kappa = 30$ and $\kappa = 1.76$.

For both types of fits the parameter T_m is held fixed. For the fits involving the Maxwellian moment-voltage relationships the value of T_m is set equal to the median (65 eV) of the best-fit Maxwellian distribution temperatures (red boxes in Figure 2e) during the marked interval. For the fits involving the kappa moment-voltage relationships the value of T_m is set equal to the median (74 eV) of the best-fit kappa distribution temperatures (blue triangles in Figure 2e). Additionally, because the experimental n values in Figure 4c are not mapped to the ionosphere, the R_B parameter in the n-V relationships (7)–(8) must be reduced by a factor $R_{B,\text{FAST}} = \frac{B_i}{B_{\text{FAST}}} \approx 4$ when fitting the experimental n-V relationship.

Similar to the process described at the beginning of this section for Monte Carlo simulation of 2-D distribution fits, to determine the range of parameters that may describe the observed moment-voltage relationships we perform fits to $N = 2{,}000$ Monte Carlo simulated moment-voltage relationships for each type of J-V, J_E-V, and n-V relationship, either Maxwellian or kappa. For each iteration, we add to each of the inferred potential drop values a uniform random number $X \sim \mathcal{N}(0, \Delta E_p)$, where the value in the second argument is the uncertainty of the electron peak energy, which arises from the EESA energy channel spacing. We insert these synthetic potential drop values into the best-fit J-V, J_E-V, and n-V relationships and add to each of these theoretical moment predictions a normal random number $Z \sim \mathcal{N}(0, 1)$ multiplied by the uncertainty of the corresponding current density, energy flux, or number density measurements. We then draw from the random variables N, R, and K, which are as described above, to initialize n_m, R_B, and κ, respectively. We then perform the fit.

The resulting joint distributions of n_m and R_B are shown in Figures 5a and 5b for the Maxwellian and kappa moment-voltage relationships, respectively. The Maxwellian moment-voltage relationships predict two different solution regimes: the first corresponds to $n_m = 0.88$–$0.90\ \text{cm}^{-3}$ and $R_B = 200$–500; the second

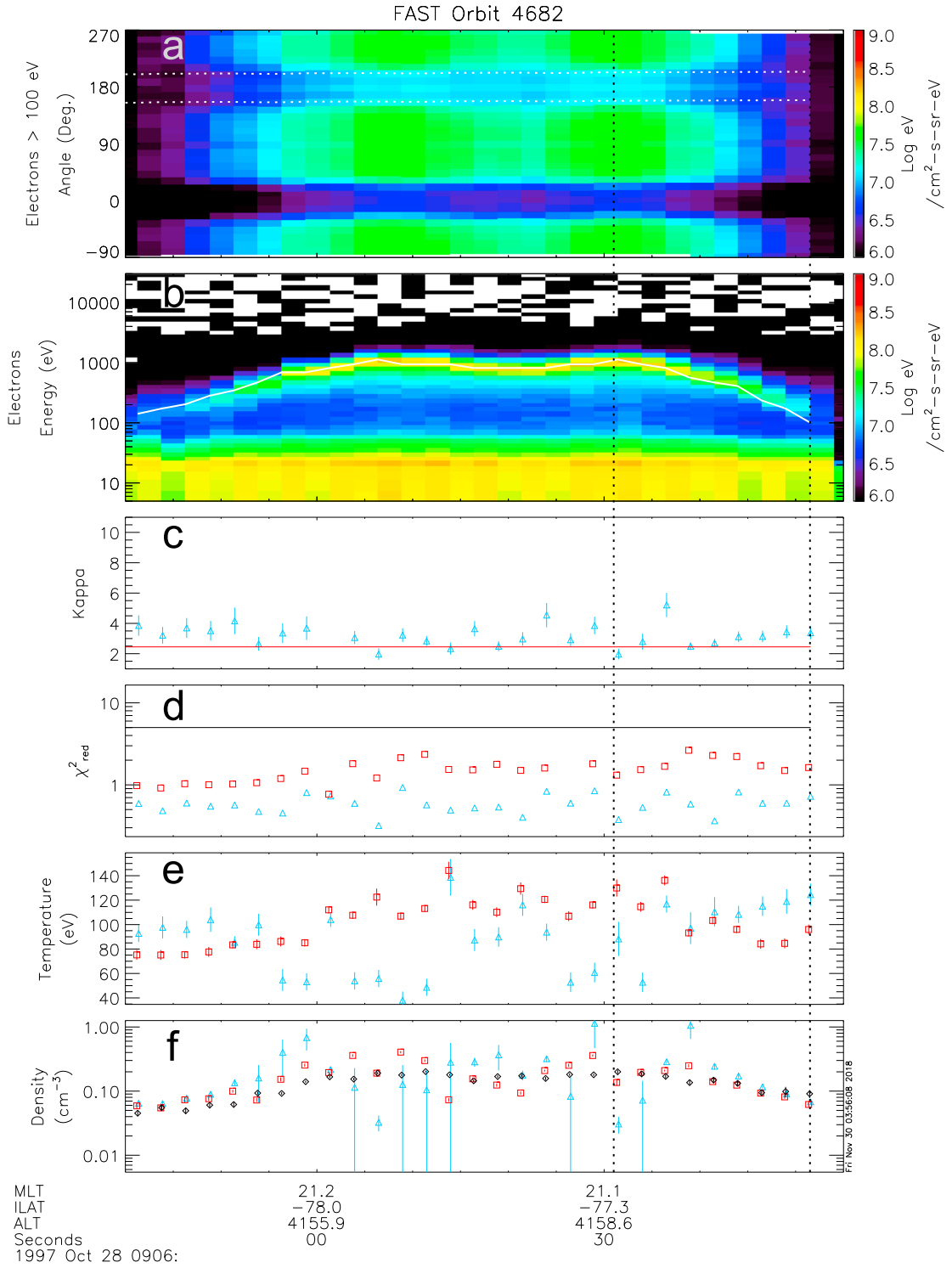

Figure 6. Electron electrostatic analyzer observations of inverted V precipitation on 28 October 1997 and corresponding 2-D fit parameters, in the same format as Figure 2. (a) >100-eV electron pitch-angle distribution. The earthward portion of the loss cone comprises the range of pitch angles between dotted horizontal lines at ~150° and ~210°. (b) Average electron energy spectrum within the earthward loss cone. (c) κ fit parameter for the best-fit kappa distribution. (d) Reduced chi-squared statistic χ^2_{red} for each fit type. (e) Best-fit temperatures. (f) Calculated and best-fit densities. Calculated densities are also obtained as model-independent moments via integration over from the energy of the channel immediately below E_p up to 5 keV, and over all pitch angles $|\theta| > 150°$. Uncertainties of calculated densities and best-fit density and temperature parameters are obtained as described in the Figure 2 caption. Electron electrostatic analyzer observations during this interval have a sample period $T = 2.5$ s. MLT = magnetic local time; ILAT = invariant latitude.

corresponds to n_m = 0.87–0.88 cm^{-3} and R_B = 3,200–7,500. The secondary axis indicates the approximate source altitudes h =5.7–7.7 R_E and h =14–15.5 R_E, respectively, where R_E indicates the radius of Earth. The kappa moment-voltage relationships also show two different solution regimes: the first corresponds to n_m = 0.70–0.79 cm^{-3}, R_B = 300—510 (h =6.4–7.7 R_E), and κ = 2.2–2.8; the second corresponds to n_m = 0.55–0.56 cm^{-3}, R_B = 300–500 (h =6.4–7.6 R_E), and $\kappa \leq 1.8$.

The χ^2_{red} value for the kappa fits in Figure 4 is 7% greater than the χ^2_{red} value for the Maxwellian fits. It therefore seems impossible to determine the correct solution regime solely on the basis of information in Figures 4 and 5. However, only the first kappa solution regime is consistent with the range κ = 2–9 that arises from direct 2-D distribution fits during the 10-s delineated period in Figure 2c.

We have also performed N = 6,000 Monte Carlo simulations using only the inferred J-V relationship (Figure 4a) and either the Maxwellian J-V relation (1) or the kappa J-V relation (4). From the Maxwellian J-V relation we obtain solutions corresponding to n_m = 0.88–0.90 cm^{-3} and $R_B \geq 680$ ($h \geq$8.5 R_E). From the kappa J-V relation (4) we obtain solutions corresponding to n_m = 0.68–0.84 cm^{-3} and $R_B \geq$ 2,100 ($h \geq$12.8 R_E) for κ = 2.2–2.8. Thus, for this case study and an assumed Maxwellian or kappa source population, the source altitude lower bound is greater when only the J-V relationship is used.

4. Orbit 4682

4.1. Data Presentation

During a 75-s interval on 28 October 1997, the FAST satellite observed inverted V electron precipitation (Figures 6a and 6b) at ~21 magnetic local time and −78° invariant latitude in the Southern Hemisphere during moderately low geomagnetic activity (K_p = 2). The pitch-angle spectrogram in Figure 6a shows that precipitation within the earthward loss cone (range of pitch angles between horizontal dotted white lines in Figure 6a) is weak ($dJ_E/dE \lesssim 5 \times 10^7$eV/cm^2-s-sr-eV), while trapped electrons over 30° $\lesssim |\theta| \lesssim$ 150° are more intense. Over the entire 75-s interval as well as over the ~20-s period between dashed lines, 09:06:31–09:06:51.5 UT, Figures 6b and 6c, respectively, show E_p = 100–1,200 eV and $\kappa \approx$ 2–5. Figure 6d shows that best-fit Maxwellian χ^2_{red} values are generally twice or more those of best-fit kappa χ^2_{red} values.

Best-fit temperatures shown in Figure 6e indicate that over the entire interval T = 75–130 ev for Maxwellian distribution fits, while T = 35–145 ev for kappa distribution fits. As with temperatures in Figure 2e, these ranges of temperatures are within the typical range for plasma sheet electrons.

Densities calculated directly from observed electron distributions in Figure 6f (black diamonds) are within the range 0.01–0.5 cm^{-3} that is typically observed in the distant plasma sheet (Kletzing et al., 2003; Paschmann et al., 2003). Most probable Maxwellian and kappa fit densities in Figure 6f tend to be with factors of 2 of the calculated densities. Similar to the density moments and uncertainties calculated in the previous section, we calculate the density over all energies from E_p up to 5 keV and over all earthward pitch angles in the Southern Hemisphere, $|\theta| > 150°$. We multiply calculated densities and density uncertainties by the solid-angle ratio $1/(1 - \cos 30°) \approx 7.46$ to compensate for the exclusion of primary electrons over the range of downgoing pitch angles dominated by trapped electrons ($90° < \theta < 150°$ and $-150° < \theta < -90°$).

Figure 7 shows an example of the electron distributions observed during the delineated period (09:06:31–09:06:51.5 UT), in the same layout as Figure 3. As in Figure 3, the best-fit kappa distribution (blue dashed line) successfully describes the suprathermal tail and is a better fit than the Maxwellian distribution (red dash-dotted line) as reflected in the χ^2_{red} values, respectively, 0.56 and 2.57 (also Figure 6d).

4.2. Inference of Magnetospheric Source Parameters

Using the Monte Carlo simulation process described in section 3.2, we now determine the range of parameters that may describe the observed moment-voltage relationships during the 20-s period shown between dashed lines in Figure 6 assuming each type of magnetospheric source population, either Maxwellian or kappa. We select this period because the inferred potential drop (solid white line in Figure 6b) decreases by roughly an order of magnitude, from ~1,150 eV to ~150 eV.

The experimental J-V, J_E-V, and n-V relationships are shown in Figures 8a–8c. Also shown are the results of simultaneously fitting all three of these relationships with the corresponding Maxwellian and kappa moment-voltage relationships (1), (4)–(8). Best-fit Maxwellian (blue lines) and kappa (orange lines) fits, respectively, correspond to χ^2_{red} = 2.5 and χ^2_{red} = 3.1. As in section 3.2, we obtain these fits by drawing from random variables $N \sim U$(0.01 cm^{-3},0.5 cm^{-3}), $R \sim U(5, 10^4)$, and $K \sim \kappa_{\min}/W$ to initialize n_m, R_B, and κ

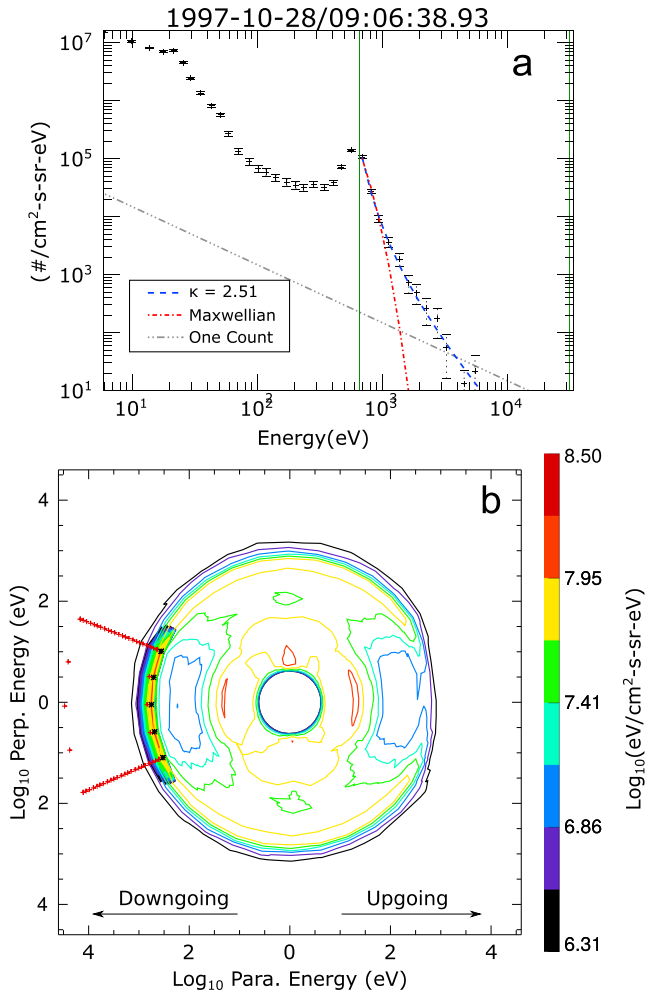

Figure 7. Electron spectra observed at 09:06:38.931–09:06:41.437 UT. The layout is the same as that of Figure 3. (a) 1-D differential number flux spectrum (black crosses) obtained by averaging all differential number flux spectra over all pitch angles within the earthward loss cone, with best-fit Maxwellian and kappa distributions overlaid (red dash-dotted line and blue dashed line, respectively). (b) Best-fit 2-D kappa distribution (solid contours) with the observed 2-D differential energy flux spectrum overlaid (contour lines). For each pitch angle black asterisks indicate the peak energy E_p = 560 eV, and red plus signs outline the range of energies and pitch angles used to perform the 2-D fit.

in each moment-voltage relationship. (The random variable K is only used in the kappa moment-voltage relationships.) For both types of fits the parameter T_m is held fixed. For the fits involving the Maxwellian moment-voltage relationships the value of T_m is set equal to the median $T = 96$ eV of the best-fit Maxwellian distribution temperatures (red boxes in Figure 6e) during the marked interval. For the fits involving the kappa moment-voltage relationships the value of T_m is set equal to the median $T = 95$ eV of the best-fit kappa distribution temperatures (blue triangles in Figure 6e).

The resulting joint distributions of n_m and R_B are shown in Figures 9a and 9b for the Maxwellian and kappa moment-voltage relationships, respectively, in a layout identical to that of Figure 5. The Maxwellian moment-voltage relationships predict n_m = 0.097–0.103 cm^{-3} and R_B ≥1,400 ($h \geq 8.1\ R_E$). The kappa moment-voltage relationships show several different solution regimes, all of which correspond to $R_B \gtrsim 370$ ($h \gtrsim 4.6\ R_E$) and n_m = 0.055–0.10 cm^{-3}: the first overlaps with the Maxwellian solution regime in Figure 9a and corresponds to n_m = 0.096–0.0102 cm^{-3}, $R_B \geq 370$ ($h \geq 4.6$), and $\kappa > 10$; the second corresponds to n_m = 0.072–0.094 cm^{-3}, $R_B \gtrsim 700$ ($h \gtrsim 5.7$), and $2 \leq \kappa$ 10; the third corresponds to n_m = 0.054–0.059 cm^{-3}, $R_B \gtrsim 103$ ($h \gtrsim 6.8$), and $\kappa < 2$.

The χ^2_{red} value for the kappa fits in Figure 8 is ~24% greater than the χ^2_{red} value for the Maxwellian fits. As with results in the previous section, information in Figures 8 and 9 seems insufficient to determine the

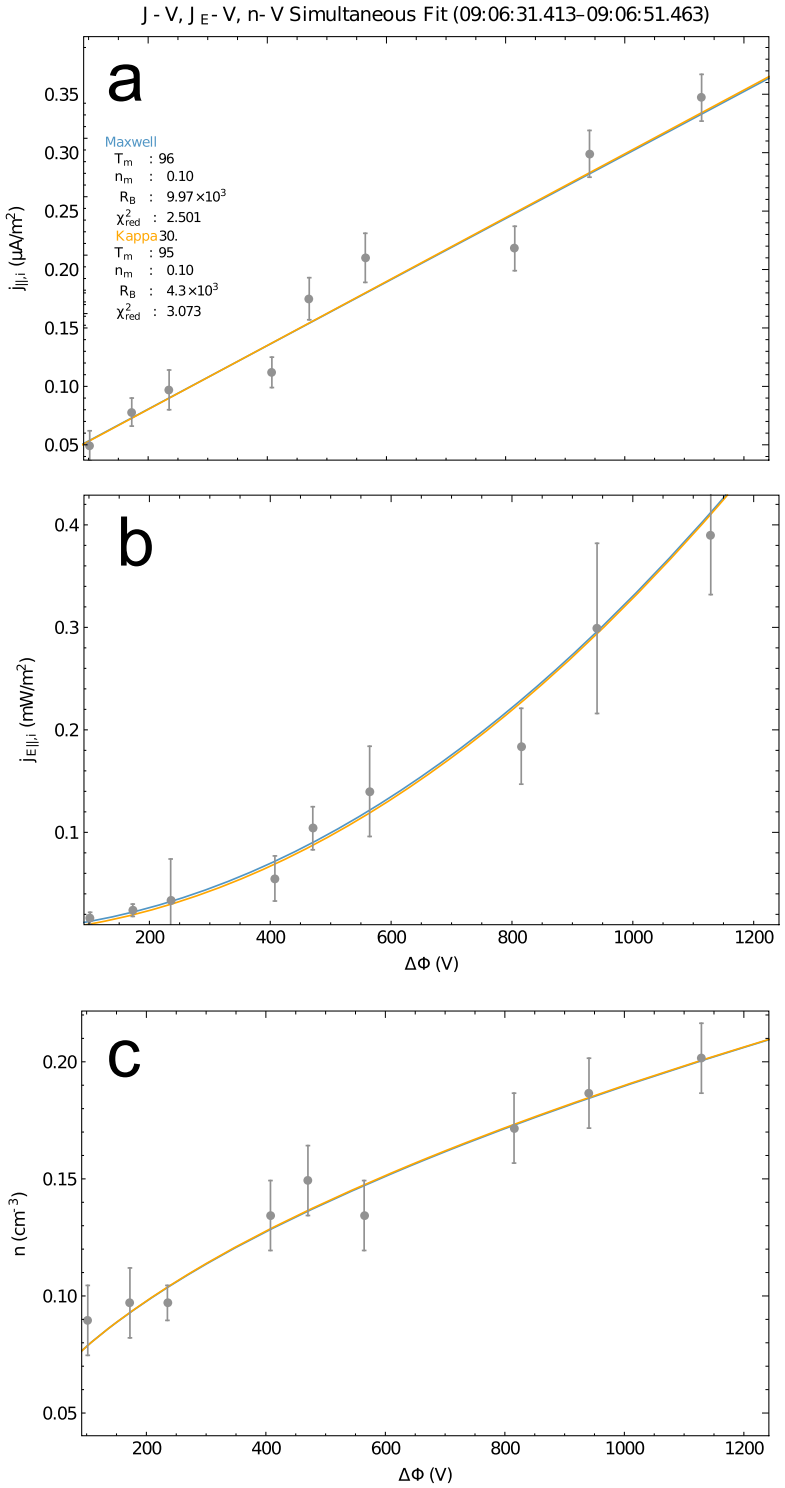

Figure 8. J-V, J_E-V, and n-V relationships inferred from electron observations during the interval 09:06:31–09:06:51.5 UT in Figure 6, together with best-fit Maxwellian (solid blue lines) and kappa (solid orange lines) moment-voltage relationships obtained by simultaneously fitting all three experimentally inferred moment-voltage relationships. The format is the same as that of Figure 4. (a) J-V relationship. (b) J_E-V relationship. (c) n-V relationship. Calculated current densities and energy fluxes (black plus signs) as well as their uncertainties (1σ) are mapped to the ionosphere at 100 km as described in section 3.2. Calculated number densities are not mapped to the ionosphere. Moment uncertainties are obtained as analytic moments of observed electron distributions (Appendix B). The χ^2_{red} values indicated in panel (a) are the sum of the χ^2_{red} values corresponding to each moment-voltage relationship. J-V = current density-voltage; J_E-V = energy flux-voltage; n-V = number density-voltage.

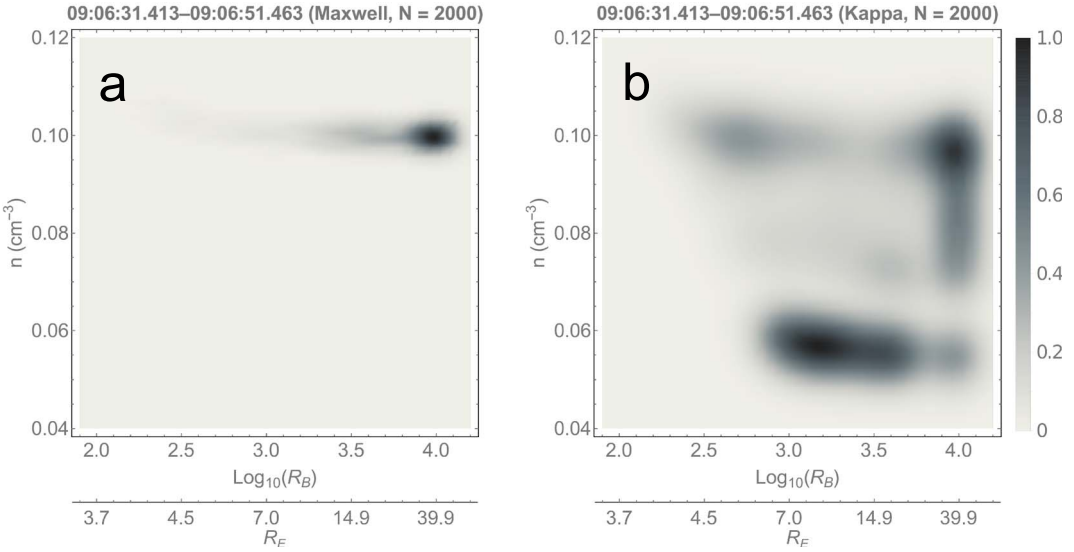

Figure 9. (a) Joint distribution of density n_m and mirror ratio R_B for Maxwellian fits of $N = 2{,}000$ Monte Carlo simulated current density-voltage, energy flux-voltage, and number density-voltage relationships (1), (5), and (7). (b) Same as panel (a), except that fits are performed using the kappa current density-voltage, energy flux-voltage, number density-voltage relationships (4), (6), and (8). In both panels the R_B axis is logarithmic and the secondary axis shows the approximate source height h. The gray scale indicates the distribution height in units such that the peak value of each distribution is 1.0.

correct solution regime. However, only the second kappa solution regime is consistent with the direct 2-D distribution fits during the 20-s delineated period in Figure 6.

As in section 3.2 we have performed $N = 6{,}000$ Monte Carlo simulations using only the inferred J-V relationship (Figure 8a) and either the Maxwellian J-V relation or the kappa J-V relation. From the Maxwellian J-V relation the resulting solutions correspond to $n_m = 0.097$–0.106 cm^{-3} and $R_B \geq 1{,}900$ ($h \geq 10\ R_E$). From the kappa J-V relation (4) we obtain solutions corresponding to $n_m = 0.071$–0.093 cm^{-3} and $R_B \geq 1{,}500$ ($h \geq 8.6\ R_E$) for $\kappa = 2$–10. Similar to results in section 3.2, the source altitude lower bound is greater when only the J-V relationship is used.

5. Discussion and Summary

For the two case studies that we have presented we assume either Maxwellian or kappa source populations when fitting the observed J-V, J_E-V, and n-V relationships, which results in χ^2_{red} values that differ by a few to several percent (see Figures 4 and 8). Such differences indicate that the moment-voltage relationships themselves are insufficient to determine the source region properties. We identify the most likely ranges of source densities and altitudes in each case study by requiring that these parameters correspond to the range of κ values estimated from direct 2-D fits of observed electron distributions.

Table 1 summarizes the ranges of most likely source parameters for both case studies. As stated in previous sections, the estimated temperatures and densities are within or near the typical ranges expected on the

Table 1
Most Likely Magnetospheric Source Parameters

	Source type	Temperature[a] (eV)	Density (cm^{-3})	R_B	h (R_E)	κ
Orbit 1607	Maxwellian	65	0.87–0.9	220–6,400	5.8–15	
	Kappa	74	0.70–0.79	300–510	6.4–7.7	2.2–2.8
Orbit 4682	Maxwellian	96	0.097–0.103	≥1400	≥8.1	
	Kappa	95	0.071–0.091	≥720	≥5.9	2–6

[a]Fixed.

basis of surveys of the plasma sheet. The combined range of κ values estimated for each orbit, $\kappa = 2$–6, are also within the ranges indicated by in situ plasma sheet surveys (Christon et al., 1989, 1991; Kletzing et al., 2003; Stepanova & Antonova, 2015).

The estimated ranges of source altitudes for these two case studies, $h = 6.4$–7.7 for Orbit 1607 observations and $h \geq 5.9\ R_E$ for Orbit 4682 observations, are above the typically quoted range of altitudes ~1.5–3 R_E for the auroral acceleration region (Mozer & Hull, 2001; Morooka et al., 2004; Marklund et al., 2011). Results from previous studies (Li et al., 2014; Wygant, 2002) indicate that such "high-altitude acceleration" scenarios often involve Alfvén wave-particle interactions, and Andersson et al. (2002) have shown that the signatures of these interactions at high altitudes may appear monoenergetic.

There are three primary limitations of this study. First, verification of the results shown in Table 1 requires conjunctive observations along similar field lines from FAST in the acceleration region and from another spacecraft in the source region; unfortunately the latter are not available during the intervals shown in Figures 2 and 6. Second, related to the previous point, the clear monoenergetic peaks in Figures 2b and 6b suggest that the potential structures above FAST are stationary relative to the transit time of plasma sheet electrons. We nevertheless cannot directly verify our assumption that quasistatic magnetospheric processes and monotonic potential structures are the cause of the electron precipitation shown in Figures 2a–2b and 6a–6b. Third, the moment-voltage relationships (1) and (4)–(8) assume that the magnetospheric source population is isotropic.

Studies performed by Hull et al. (2010) and Marklund et al. (2011) have shown that potential structures are generally neither quasistatic nor monotonic, and Hatch et al. (2018) present statistics suggesting that electron distributions may be modified in the vicinity of the AAR. These studies indicate that our assumptions of stationarity, nonvariability of source parameters along the mapped satellite track, and adiabatic transport from the source region to the ionosphere are not always true, and some evidence of violation of our assumptions appears in, for example, the experimental J-V relation (top panel) in Figure 4: For some data points neither the Maxwellian nor the kappa J-V relation is within 2–3σ. Such differences could suggest that the errors associated with our assumptions are larger than that associated with moment uncertainty and counting statistics.

Concerning the third limitation, magnetospheric source populations are not necessarily isotropic, and previous studies (Forsyth et al., 2012; Marghitu et al., 2006) have shown how the observed degree of anisotropy of electron precipitation may in fact be used to estimate the source altitude. While outside the scope of the present study, relaxing the assumption of isotropy and adapting the source altitude estimation techniques presented by these previous studies are natural future extensions of the techniques we have developed for the two case studies presented above.

Regardless of the particular values or ranges of parameters that we have identified, these case studies nevertheless demonstrate how the non-Maxwellian nature of an electron source population may be embedded in the observed moment-voltage relationships, requiring modification of both the inferred source density and mirror ratio. From this standpoint the degree to which a source population departs from thermal equilibrium, as indicated by the κ parameter in this study, is as fundamental a plasma property as density or temperature.

A relatively small number of studies, such as those of Dombeck et al. (2013), Lu et al. (1991), Morooka et al. (2004), and Shiokawa et al. (1990), has compared various forms of the Knight relation (1) to observations. To our knowledge, however, no study besides the present has used the moment-voltage relationships (1) and (4)–(8) that are predicted by Liouville's theorem, or any subset thereof, to infer the properties of the magnetospheric source region on the basis of observations at lower altitudes.

In summary, in this study we have (i) derived the two previously unpublished n-V relationships (7) and (8); (ii) inferred the properties of magnetospheric source populations in two case studies based on simultaneous fitting of the three experimental moment-voltage relationships with corresponding theoretical moment-voltage relationships (1), (4)–(8), moment uncertainties, and direct 2-D fits of observed precipitating electron distributions; (iii) demonstrated that knowledge of the degree to which monoenergetic precipitation departs from Maxwellian form, which we parameterize via the κ index, is required to determine the most likely set of magnetospheric source parameters.

Appendix A: Theory of Collisionless Transport Through a Field-Aligned Monotonic Potential Structure

Here we review the theory that yields the J-V, J_E-V, and n-V relationships (1) and (4)–(8). The development is intended to be brief since several more elaborate developments have been given elsewhere (e.g., references in section 1).

Assuming a gyrotropic, collisionless magnetospheric source population, an electron distribution function $f(v_\parallel, v_\perp)$ can be written in terms of total energy and the first adiabatic invariant:

$$E = \frac{m_e}{2}(v_\parallel^2 + v_\perp^2) + \Pi(B); \tag{A1a}$$

$$\mu = \frac{m_e v_\perp^2}{2B(s)}. \tag{A1b}$$

In these expressions $v_\parallel$ and $v_\perp$ are parallel and perpendicular velocity, $\Pi(B)$ is the distribution of potential energy along the field line, $B(s)$ is magnetic field strength, and s is a one-to-one function of B that measures the distance along a magnetic field line from the magnetospheric source region toward the ionosphere. We denote the magnetic field strength at the source $B_m \equiv B(s_0)$ and assume $\Pi(B_m) = 0$. Thus, the initial total energy is $E_0 = \frac{m_e}{2}(v_{\parallel,0}^2 + v_{\perp,0}^2)$. From equations (A1) we then have $v_{\parallel,0}^2 = v_\parallel^2 + v_\perp^2\left(1 - \frac{B_m}{B(s)}\right) + \frac{2}{m_e}\Pi(B)$, with $v_{\perp,0}^2$ eliminated via equation (A1b).

In principle derivation of a moment-voltage relationship involves simple application of equations (A1) in Liouville's theorem, $f(v_\parallel, v_\perp) = f(v_{\parallel,0}, v_{\perp,0})$, followed by calculation of the relevant moment. In practice, the complexity of these calculations is related to the shape of $\Pi(B)$, since multiple regions of phase space may be inaccessible, or "forbidden," at lower altitudes. (For example, particles with parallel velocities that are too low to overcome a retarding potential structure will be reflected.) Care must be taken to exclude such forbidden regions from moment calculations (Boström, 2003, 2004; Liemohn & Khazanov, 1998; Pierrard et al., 2007). We are interested in the simplest nontrivial case, namely, that for which $\Pi(B)$ obeys the conditions $\frac{d\Pi}{dB} < 0$ and $\frac{d^2\Pi}{dB^2} > 0$, with the derivatives defined everywhere along the magnetic field line. For this case each moment-voltage relationship is independent of the shape of $\Pi(B)$ and can be written as a function of the total potential difference $\Delta\Phi$ (e.g., the J-V relationships (1) and (4); see Liemohn & Khazanov, 1998).

The allowed region of phase space is $v_\parallel \geq 0$. Via the two invariants in equation (A1) the lower bound of this inequality may be written in terms of total kinetic energy W, initial parallel kinetic energy $W_{\parallel,0}$, and pitch angle $\theta \equiv \tan^{-1}(v_\perp/v_\parallel)$ as

$$W_{\parallel,0} = W\left(1 - \sin^2(\theta)\frac{B_m}{B(s)}\right) - e\Delta\Phi = 0.$$

The region of phase space over which to integrate is then defined by the inequalities

$$W \geq e\Delta\Phi / \left(1 - \sin^2(\theta)\frac{B_m}{B(s)}\right); \tag{A2a}$$

$$\theta \in \begin{cases} (-90°, 90°) & \text{Northern Hemisphere;} \\ (90°, 270°) & \text{Southern Hemisphere.} \end{cases} \tag{A2b}$$

Assuming gyrotropy the zeroth moment of $f(v_\parallel, v_\perp)$ is $n = 2\pi \int\int v_\perp f(v_\parallel, v_\perp) dv_\perp dv_\parallel$. The Maxwellian and kappa n-V relations (7) and (8) result from evaluation of this integral over the boundaries (A2) using either an isotropic Maxwellian or isotropic kappa distribution function, respectively, and assuming a total potential drop $\Delta\Phi$.

For $1 \lesssim \bar{\phi} \ll R_B$ the Maxwellian n-V relation (7) reduces to

$$n/n_m = \frac{1}{2}e^{\bar{\phi}}\mathrm{erfc}\,\bar{\phi}^{\frac{1}{2}} + \left(\bar{\phi}/\pi\right)^{\frac{1}{2}}, \tag{A3}$$

while in the limit $\bar{\phi} \gg R_B > 1$ the Maxwellian n-V relation reduces to

$$n/n_m = \frac{1}{2} e^{\bar{\phi}} \mathrm{erfc}\, \bar{\phi}^{\frac{1}{2}} + \frac{1}{2} \frac{R_B - 1}{\left(\pi \bar{\phi}\right)^{\frac{1}{2}}}. \tag{A4}$$

For fixed R_B the maximum value of n/n_m is given by $\bar{\phi}$ such that

$$e^{\bar{\phi}} \mathrm{erfc}\left(\sqrt{\bar{\phi}}\right) = \frac{2}{\sqrt{\pi\left(R_B - 1\right)}} D\left(\sqrt{\frac{\bar{\phi}}{R_B - 1}}\right). \tag{A5}$$

Appendix B: Analytic Expressions for Moment Uncertainties

We follow the Gershman et al. (2015) framework for calculating the moment uncertainties used in Monte Carlo simulations in sections 3.2 and 4.2. Let W be a differentiable function of plasma moments $\langle nA_i \rangle$; the linearized uncertainty σ_W may be expressed

$$\sigma_W^2 = \sum_i \sum_j \left(\frac{\partial W}{\partial A_i}\right)\left(\frac{\partial W}{\partial A_j}\right) \sigma_{A_i, A_j}. \tag{B1}$$

The squared uncertainty of n is trivially σ_n^2, while squared uncertainties of $j_\parallel$ and $j_{E\parallel}$ are

$$\sigma_{j_\parallel}^2 = V_\parallel \sigma_n^2 + n\sigma_{V_\parallel}^2 + \sigma_{n, V_\parallel}; \tag{B2a}$$

$$\sigma_{j_{E\parallel}}^2 = \sigma_{H,\parallel}^2 + B\left[2\sigma_{H_\parallel, V_\parallel} + B\sigma_{V_\parallel}^2\right] \tag{B2b}$$

$$+V_\parallel \left[3\sigma_{H_\parallel, P_\parallel} + 2\sigma_{H_\parallel, P_\perp} + B\left(3\sigma_{V_\parallel, P_\parallel} + 2\sigma_{V_\parallel, P_\perp}\right)\right] \tag{B2c}$$

$$+V_\parallel^2 \left[\frac{9}{4}\sigma_{P_\parallel}^2 + 3\sigma_{P_\parallel, P_\perp} + \sigma_{P_\perp}^2\right]; \tag{B2d}$$

where $V_\parallel$ is the average parallel velocity and $B = \left(\frac{3}{2}P_\parallel + P_\perp\right)$ in expression (B2d). Equation (B2d) expresses $\sigma_{j_{E\parallel}}^2$ in terms of parallel heat flux $H_\parallel$ and parallel and perpendicular pressures $P_\parallel$ and $P_\perp$. Dependence on $H_\parallel$ arises because the computational routine provided as supporting information for Gershman et al. (2015) yields uncertainties and covariances related to the heat flux vector $\mathbf{H}$; with this dependence the parallel energy flux $j_{E\parallel}$ can be written $j_{E\parallel} = H_\parallel + V_\parallel\left(\frac{3}{2}P_\parallel + P_\perp\right)$ (Paschmann & Daly, 1998). Equation (B2d) also assumes (i) gyrotropy, because FAST ion and electron ESAs measure only one direction perpendicular to the geomagnetic field, and (ii) average perpendicular velocity $V_\perp = 0$, since there is negligible dependence on $V_\perp$ at FAST altitudes.

Calculation of moment uncertainties and covariances from $f(\mathbf{v})$ in equations (B2) requires the following assumptions:

1. The sampling of each phase space volume is unique. For FAST ESAs, which sample energy and pitch angle, this assumption means, for example, that there is no overlap between regions of phase space sampled by each energy-angle detector bin, and that there is no crosstalk.
2. The sampled phase space density $f(\mathbf{v})$ corresponds to a number of counts $N(\mathbf{v}) = f(\mathbf{v})\Delta V(\mathbf{v})\Delta X(\mathbf{v})$, where $\Delta V(\mathbf{v})$ and $\Delta X(\mathbf{v})$ are, respectively, the phase space velocity and position volumes sampled by FAST ESAs, and $N(\mathbf{v})$ is a Poisson-distributed random variable.

The covariance between moments $\langle nA_i \rangle$ and $\langle nA_j \rangle$ is $\sigma_{\langle nA_i \rangle, \langle nA_j \rangle} = E\left[\langle nA_i \rangle \langle nA_j \rangle\right] - E\left[\langle nA_i \rangle\right] E\left[\langle nA_j \rangle\right]$, where E denotes the expectation value such that

$$\begin{aligned} E\left[\langle nA_i \rangle \langle nA_j \rangle\right] &= \iiint \mathbf{d}^3\mathbf{v} A_i(\mathbf{v}) \iiint \mathbf{d}^3\mathbf{v}' A_j(\mathbf{v}') E\left[f(\mathbf{v}) f(\mathbf{v}')\right]; \\ E\left[\langle nA_i \rangle\right] E\left[\langle nA_j \rangle\right] &= \iiint \mathbf{d}^3\mathbf{v} A_i(\mathbf{v}) \iiint \mathbf{d}^3\mathbf{v}' A_j(\mathbf{v}') E\left[f(\mathbf{v})\right] E\left[f(\mathbf{v}')\right]. \end{aligned} \tag{B3}$$

It follows that $\sigma_{\langle nA_i\rangle,\langle nA_j\rangle} = \iiint \mathbf{d}^3\mathbf{v}A_i(\mathbf{v}) \iiint \mathbf{d}^3\mathbf{v}'A_j(\mathbf{v}')\sigma_{f(\mathbf{v}),f(\mathbf{v}')}$; that is, the covariance between any two moments of $f(\mathbf{v})$ depends on the covariance between the points in phase space $\mathbf{v}$ and v'. Gershman et al. (2015) show that if $\sigma'_{f(\mathbf{v}),f(v)}$) is written in terms of the correlation between regions of phase space,

$$\sigma_{f(\mathbf{v}),f(\mathbf{v}')} = \sigma_{f(\mathbf{v})}\sigma_{f(\mathbf{v}')}r(\mathbf{v},\mathbf{v}'), \tag{B4}$$

the first assumption implies $r(\mathbf{v},v') \approx \delta'_{\mathbf{v}v}$, while the second assumption implies that the uncertainty of the sampled phase space density is $\sigma_{f(\mathbf{v})} = f(\mathbf{v})/\sqrt{N(\mathbf{v})}$. Thus,

$$\sigma_{f(\mathbf{v}),f(\mathbf{v}')} \approx \frac{f^2(\mathbf{v})}{N(\mathbf{v})}, \tag{B5}$$

which leads to the analytic expression

$$\sigma_{\langle nA_i\rangle,\langle nA_j\rangle} \approx \iiint \left(\mathbf{d}^3\mathbf{v}\right)^2 A_i(\mathbf{v})A_j(\mathbf{v})\frac{f^2(\mathbf{v})}{N(\mathbf{v})} = \left\langle nA_iA_j\left(\mathbf{d}^3\mathbf{v}\right)\frac{f(\mathbf{v})}{N(\mathbf{v})}\right\rangle, \tag{B6}$$

where the RHS of (B6) represents $\sigma_{\langle nA_i\rangle,\langle nA_j\rangle}$ as a moment of $f(\mathbf{v})$.

Acknowledgments
All observations and measurements made by the FAST spacecraft are available as a Level 1 data product through SDT (http://sprg.ssl.berkeley.edu/~sdt/SdtReleases.html). We are grateful to Craig Markwardt for making publicly available MPFIT (http://cow.physics.wisc.edu/~craigm/idl/fitting.html), the Interactive Data Language version of the MINPACK-1 fitting routines, which we have used extensively in this research. Work at the Birkeland Center for Space Science and the University of Bergen was funded by the Research Council of Norway/CoE under contract 223252/F50. Work at Dartmouth College was supported by NASA Headquarters under NASA grant NNX17AF92G and sub-award W000726838 to NASA grant NNX15AL08G. Work at Space Sciences Laboratory was supported by NASA grants NNX15AF57G and NNX16AG69G.

References

Andersson, L., Ivchenko, N., Clemmons, J., Namgaladze, A. A., Gustavsson, B., Wahlund, J. E., et al. (2002). Electron signatures and Alfvén waves. *Journal of Geophysical Research*, *107*(A9), 1244.

Boström, R. (2003). Kinetic and space charge control of current flow and voltage drops along magnetic flux tubes: Kinetic effects. *Journal of Geophysical Research*, *108*(A4), 8004. https://doi.org/10.1029/2002JA009295

Boström, R. (2004). Kinetic and space charge control of current flow and voltage drops along magnetic flux tubes: 2. Space charge effects. *Journal of Geophysical Research*, *109*, A01208. https://doi.org/10.1029/2003JA010078

Carlson, C. W., Mcfadden, J. P., Turin, P., Curtis, D. W., & Magoncelli, A. (2001). The electron and ion plasma experiment for FAST. *Space Science Reviews*, *98*(1), 33–66. https://doi.org/10.1023/A:1013139910140

Chiu, Y. T., & Schulz, M. (1978). Self-consistent particle and parallel electrostatic field distributions in the magnetospheric-ionospheric auroral region. *Journal of Geophysical Research*, *83*(A2), 629–642. https://doi.org/10.1029/JA083iA02p00629

Christon, S. P., Williams, D. J., Mitchell, D. G., Frank, L. A., & Huang, C. Y. (1989). Spectral characteristics of plasma sheet ion and electron populations during undisturbed geomagnetic conditions. *Journal of Geophysical Research*, *94*(A10), 13409. https://doi.org/10.1029/JA094iA10p13409

Christon, S. P., Williams, D. J., Mitchell, D. G., Huang, C. Y., & Frank, L. A. (1991). Spectral characteristics of plasma sheet ion and electron populations during disturbed geomagnetic conditions. *Journal of Geophysical Research*, *96*(A1), 1–22. https://doi.org/10.1029/90JA01633

Cowley, S. W. H. (2000). Magnetosphere-ionosphere interactions: A tutorial review. In S.-I. Ohtani, R. Fujii, M. Hesse, & R. L. Lysak (Eds.), *Magnetospheric current systems* (Vol. 118, pp. 91–106). Washington, DC: American Geophysical Union. https://doi.org/10.1029/GM118p0091

Dombeck, J., Cattell, C., & McFadden, J. (2013). A FAST study of quasi-static structure ("Inverted-V") potential drops and their latitudinal dependence in the premidnight sector and ramifications for the current-voltage relationship. *Journal of Geophysical Research: Space Physics*, *118*, 5731–5741. https://doi.org/10.1002/jgra.50532

Dors, E. E., & Kletzing, C. A. (1999). Effects of suprathermal tails on auroral electrodynamics. *Journal of Geophysical Research*, *104*(A4), 6783–6796. https://doi.org/10.1029/1998JA900135

Elphic, R. C., Bonnell, J. W., Strangeway, R. J., Kepko, L., Ergun, R. E., McFadden, J. P., et al. (1998). The auroral current circuit and field-aligned currents observed by FAST. *Geophysical Research Letters*, *25*(12), 2033–2036. https://doi.org/10.1029/98GL01158

Forsyth, C., Fazakerley, A. N., Walsh, A. P., Watt, C. E. J., Garza, K. J., Owen, C. J., et al. (2012). Temporal evolution and electric potential structure of the auroral acceleration region from multispacecraft measurements. *Journal of Geophysical Research*, *117*, A12203. https://doi.org/10.1029/2012JA017655

Gershman, D. J., Dorelli, J. C., F.-Viñas, A., & Pollock, C. J. (2015). The calculation of moment uncertainties from velocity distribution functions with random errors. *Journal of Geophysical Research: Space Physics*, *120*, 6633–6645. https://doi.org/10.1002/2014JA020775

Hatch, S. M., Chaston, C. C., & LaBelle, J. (2018). Nonthermal limit of monoenergetic precipitation in the auroral acceleration region. *Geophysical Research Letters*, *45*, 10,167–10,176. https://doi.org/10.1029/2018GL078948

Hull, A. J., Wilber, M., Chaston, C. C., Bonnell, J. W., McFadden, J. P., Mozer, F. S., et al. (2010). Time development of field-aligned currents, potential drops, and plasma associated with an auroral poleward boundary intensification. *Journal of Geophysical Research*, *115*, A06211. https://doi.org/10.1029/2009JA014651

Janhunen, P., & Olsson, A. (1998). The current-voltage relationship revisited: Exact and approximate formulas with almost general validity for hot magnetospheric electrons for bi-Maxwellian and kappa distributions. *Annals of Geophysics*, *16*(3), 292–297.

Kaeppler, S. R., Nicolls, M. J., Strømme, A., Kletzing, C. A., & Bounds, S. R. (2014). Observations in the E region ionosphere of kappa distribution functions associated with precipitating auroral electrons and discrete aurorae. *Journal of Geophysical Research: Space Physics*, *119*, 10,164–10,183. https://doi.org/10.1002/2014JA020356

Karlsson, T. (2012). The acceleration region of stable auroral arcs. In A. Keiling, E. Donovan, F. Bagenal, & T. Karlsson (Eds.), *Auroral phenomenology and magnetospheric processes: Earth and other planets* (Vol. 197, pp. 227–240). Washington, DC: American Geophysical Union. https://doi.org/10.1029/2011GM001179

Kletzing, C. A., Scudder, J. D., Dors, E. E., & Curto, C. (2003). Auroral source region: Plasma properties of the high-latitude plasma sheet. *Journal of Geophysical Research*, *108*(A10), 1360. https://doi.org/10.1029/2002JA009678

Knight, S. (1973). Parallel electric fields. *Planetary and Space Science*, *21*, 741–750.

Li, B., Marklund, G., Alm, L., Karlsson, T., Lindqvist, P.-A., & Masson, A. (2014). Statistical altitude distribution of Cluster auroral electric fields, indicating mainly quasi-static acceleration below 2.8 RE and Alfvénic above. *Journal of Geophysical Research: Space Physics*, *119*, 8984–8991. https://doi.org/10.1002/2014JA020225

Liemohn, M. W., & Khazanov, G. V. (1998). Collisionless plasma modeling in an arbitrary potential energy distribution. *Physics of Plasmas*, *5*(3), 580–589. https://doi.org/10.1063/1.872750

Livadiotis, G., & McComas, D. J. (2010). Exploring transitions of space plasmas out of equilibrium. *The Astrophysical Journal*, *714*(1), 971–987.

Lu, G., Reiff, P. H., Burch, J. L., & Winningham, J. D. (1991). On the auroral current-voltage relationship. *Journal of Geophysical Research*, *96*(A3), 3523. https://doi.org/10.1029/90JA02462

Lyons, L. R., Koskinen, H. E. J., Blake, J. B., Egeland, A., Hirahara, M., Øieroset, M., et al. (1999). Processes leading to plasma losses into the high-latitude atmosphere. In B. Hultqvist, M. Øieroset, G. Paschmann, & R. A. Treumann (Eds.), *Magnetospheric plasma sources and losses final rep. issi study proj. source loss process* (pp. 85–135). Dordrecht, Netherlands: Springer. https://doi.org/10.1007/978-94-011-4477-3

Marghitu, O., Klecker, B., & McFadden, J. P. (2006). The anisotropy of precipitating auroral electrons: A FAST case study. *Advances in Space Research*, *38*(8), 1694–1701.

Marklund, G. T., Sadeghi, S., Karlsson, T., Lindqvist, P.-A., Nilsson, H., Forsyth, C., et al. (2011). Altitude distribution of the auroral acceleration potential determined from Cluster satellite data at different heights. *Physical Review Letters*, *106*(5), 55002. https://doi.org/10.1103/PhysRevLett.106.055002

Moore, T. E., Pollock, C. J., & Young, D. T. (1998). Kinetic core plasma diagnostics. In R. F. Pfaff, J. E. Borovsky, & D. T. Young (Eds.), *Measurement techniques in space plasmas—Particles, Geophysical Monograph Series* (Vol. 102, pp. 105–123). Washington, DC: American Geophysical Union. https://doi.org/10.1029/GM102p0105

Morooka, M., Mukai, T., & Fukunishi, H. (2004). Current-voltage relationship in the auroral particle acceleration region. *Annales Geophysicae*, *22*(10), 3641–3655.

Mozer, F. S., & Hull, A. (2001). Origin and geometry of upward parallel electric fields in the auroral acceleration region. *Journal of Geophysical Research*, *106*(A4), 5763–5778. https://doi.org/10.1029/2000JA900117

Nicholls, D. C., Dopita, M. A., & Sutherland, R. S. (2012). Resolving the electron temperature discrepancies in H II regions and planetary nebulae: κ-distributed electrons. *The Astrophysical Journal*, *752*(2), 148.

Ogasawara, K., Livadiotis, G., Grubbs, G. A., Jahn, J.-M., Michell, R., Samara, M., et al. (2017). Properties of suprathermal electrons associated with discrete auroral arcs. *Geophysical Research Letters*, *44*, 3475–3484. https://doi.org/10.1002/2017GL072715

Paschmann, G., & Daly, P. W. (1998). Analysis methods for multi-spacecraft data. ESA Publications Division, Keplerlaan vol. 1.

Paschmann, G., Haaland, S., & Treumann, R. (Eds.) (2003). Theoretical building blocks, *Auroral plasma physics* (pp. 41–92). Dordrecht, Netherlands: Springer. https://doi.org/10.1007/978-94-007-1086-3

Pierrard, V. (1996). New model of magnetospheric current-voltage relationship. *Journal of Geophysical Research*, *101*(A2), 2669–2675. https://doi.org/10.1029/95JA00476

Pierrard, V., Khazanov, G. V., & Lemaire, J. F. (2007). Current–voltage relationship. *Journal of Atmospheric and Solar-Terrestrial Physics*, *69*(16), 2048–2057.

Pierrard, V., & Lazar, M. (2010). Kappa distributions: Theory and applications in space plasmas. *Solar Physics*, *267*(1), 153–174. https://doi.org/10.1007/s11207-010-9640-2

Press, W., Teukolsky, S., Vetterling, W., & Flannery, B. (2007). *Numerical recipes 3rd edition: The art of scientific computing*. New York: Cambridge University Press.

Shiokawa, K., Fukunishi, H., Yamagishi, H., Miyaoka, H., Fujii, R., & Tohyama, F. (1990). Rocket observation of the magnetosphere-ionosphere coupling processes in quiet and active arcs. *Journal of Geophysical Research*, *95*(A7), 10679. https://doi.org/10.1029/JA095iA07p10679

Stepanova, M., & Antonova, E. E. (2015). Role of turbulent transport in the evolution of the κ distribution functions in the plasma sheet. *Journal of Geophysical Research: Space Physics*, *120*, 3702–3714. https://doi.org/10.1002/2014JA020684

Temerin, M. (1997). What do we really know about auroral acceleration? *Advances in Space Research*, *20*(415), 1025–1035.

Treumann, R. A. (1999a). Generalized-Lorentzian thermodynamics. *Physica Scripta*, *59*(3), 204–214.

Treumann, R. A. (1999b). Kinetic theoretical foundation of Lorentzian statistical mechanics. *Physica Scripta*, *59*(1), 19–26.

Vasyliūnas, V. M. (1968). A survey of low-energy electrons in the evening sector of the magnetosphere with OGO 1 and OGO 3. *Journal of Geophysical Research*, *73*, 2839–2884.

Wing, S., & Newell, P. T. (1998). Central plasma sheet ion properties as inferred from ionospheric observations. *Journal of Geophysical Research*, *103*(A4), 6785–6800. https://doi.org/10.1029/97JA02994

Wygant, J. R. (2002). Evidence for kinetic Alfvén waves and parallel electron energization at 4–6 R_E altitudes in the plasma sheet boundary layer. *Journal of Geophysical Research*, *107*(A8), 1201.